ISSN 8756-6990, Optoelectronics, Instrumentation and Data Processing, 2010, Vol. 46, No. 4, pp. 329–339. © Allerton Press, Inc., 2010.
Original Russian Text © W. Osten, B. Dörband, E. Garbusi, C. Pruss, L. Seifert, 2010, published in Avtometriya, 2010, Vol. 46, No. 4, pp. 40–53.

NANOTECHNOLOGIES
IN OPTICS AND ELECTRONICS

Testing Aspheric Lenses: New Approaches

W. Osten[a], B. Dörband[b], E. Garbusi[a], Ch. Pruss[a], and L. Seifert[a]

[a]*Universität Stuttgart, Institut für Technische Optik,*
Pfaffenwaldring 9, D-70569 Stuttgart, Germany
E-mail: osten@ito.uni-stuttgart.de
[b]*Carl Zeiss SMT AG,*
Rudolf-Eber-Strasse 2, 73447 Oberkochen, Germany

Received February 18, 2010

Abstract—Optical metrology provides a unique approach to measuring surfaces, both technical and optical, over a wide measurement range from macro to nano. We present two new approaches to measuring aspheric lenses with increased flexibility. The first is based on a modified Twyman–Green interferometer where multiple sources for the illumination of the aspheric surface with different angles are adopted to achieve a local compensation of the gradient and consequently a reduction of interference fringes. The second is based on a chromatic Fizeau interferometer with a diffractive element as null-optic for the measurement of extreme ultraviolet aspheres.

DOI: 10.3103/S8756699010040059

Key words: optical metrology, asphere testing, dynamic wavefront adaption, dynamic wavelength adaption.

INTRODUCTION

Aspheric lenses have become synonymous with high-performance optics. In fact, many lens vendors have made their aspheric elements a prominent part of their advertising campaigns. Aspheres are increasingly being used in optical systems for all kinds of applications, with varying degrees of asphericities and accuracy requirements. In comparison to the classical design, where only spherical surfaces are used, aspherical elements make it possible to generate almost any desired wavefront and allow the correction of aberrations in optical systems with increased flexibility and with fewer elements. Thus optical designers are continuously working on new design concepts but are simultaneously challenged to develop new approaches for making and measuring them. Due to the extreme freedom in their design, there is no standard technique to test them. However, especially such technologies are wanted that combine accuracy with flexibility.

In that paper current developments such as mechanically free solutions based on nonstandard illumination concepts are discussed. The first takes advantage of an array of coherent point sources to generate simultaneously many testing wavefronts [1–3] while the second makes use of a chromatization within a Fizeau interferometer by using a diffractive element as null-optic for the measurement of extreme ultraviolet (EUV) aspheres [4].

TESTING ASPHERIC LENSES WITH MULTIPLE ILLUMINATION SOURCES

A common problem in interferometric testing of aspheres is the extremely high fringe density produced by aspheric elements unable to be resolved by an image sensor. This problem arises due to the high gradients of the surfaces under test which introduce a strong wavefront deviation between the test and reference arms of the interferometer. Consequently, the dynamic range of the interferometer is often limited by two effects: the extremely high interference fringe density and vignetting artifacts. There are several available techniques to overcome these limitations. State of the art is to use a null optic such as a computer generated hologram (CGH) as a compensation element in the test arm of the interferometer in order to reduce or fully eliminate the strong wavefront deviation caused by the surface under test [5–7]. These elements are extremely flexible

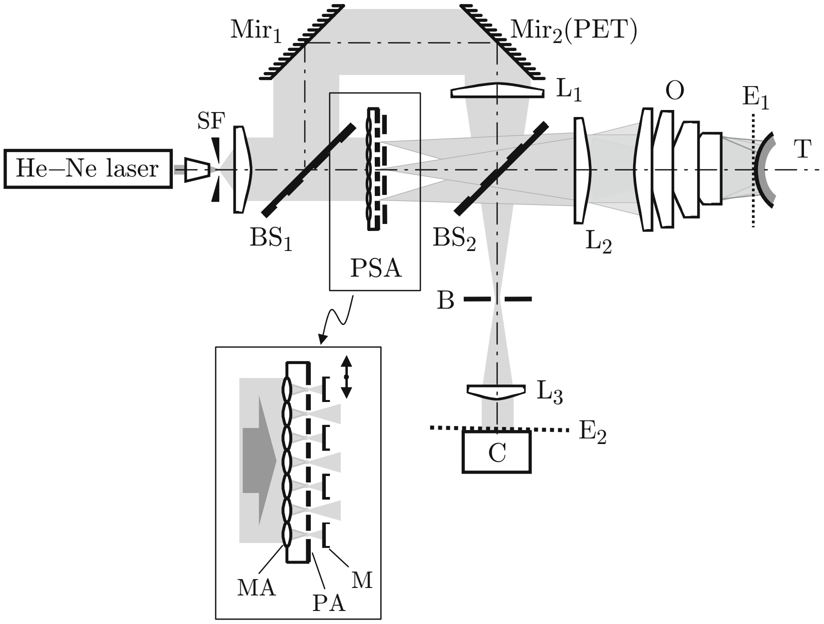

Fig. 1. Experimental setup.

and can be used to test a wide range of aspheric and freeform elements. On the other hand, one of the main drawbacks is related to their costs and the necessary time for their fabrication. Each new type of aspheric element requires the fabrication of a new CGH. Another approach to reducing the fringe density is to move either the asphere or the optics of the interferometer [8, 9] generating evaluable interferogram subapertures of the asphere. This involves precisely controlled mechanical movements and many subsequent measurements. Further arrangements for non-null interferometry and measurement of aspheres without compensator are proposed in [10–13].

In order to avoid the movement of the asphere, recently a solution was proposed [14] where the reference beam of the interferometer is manipulated to compensate the wavefront deviations present in the test arm of the interferometer. This interferometer with a dynamic reference beam allows for an extended measurement range but a high numerical aperture in the imaging optics of the interferometer is also required to avoid vignetting effects in case of higher asphericity.

Here a new approach based on a modified Twyman–Green interferometer is presented [13, 15]. The solution adopts multiple sources for the illumination of the aspheric surface with different angles, achieving in this way a local compensation of the gradient and consequently a reduction of interference fringes. During the measurement process, different sources are activated while the reference beam remains fixed. This configuration makes it possible to deal with strong aspheric departures avoiding at the same time vignetting artifacts and high fringe densities on the detector. The method requires no mechanical motion of the test part and allows one to activate multiple sources simultaneously making the measurement time extremely short compared to the available techniques mentioned above.

Such a non-null test configuration without a wavefront compensator increases the measurement flexibility. However, since the incidence of the test wavefront is no longer normal to the test surface, the interferometer has to be well characterized to correct errors that result from this mismatch in optical paths. Since the path followed by the test beam is in general quite different from the one followed by the reference beam (no common-path configuration), we have to be able to distinguish additional aberrations from the contributions due to the surface being tested. Furthermore, due to the high gradients of the tested surfaces, the fringe density increases beyond the limit that the image sensor is able to resolve and effects such as the vignetting of the wavefront must also be taken into consideration.

The interferometer is depicted in Fig. 1, where Mir$_1$ and Mir$_2$ are fold mirrors, PET is a piezo-electric transducer, M is the source selection mask, T is the test surface, E$_1$ is the plane corresponding to the vertex of the test element, E$_2$ iss the position of the camera C. The basic configuration is a Twyman–Green interferometer with a modification in the test arm of the interferometer. A He–Ne-laser source (λ = 632.8 nm) is filtered by means of a spatial filter (SF) and is then collimated and split into the

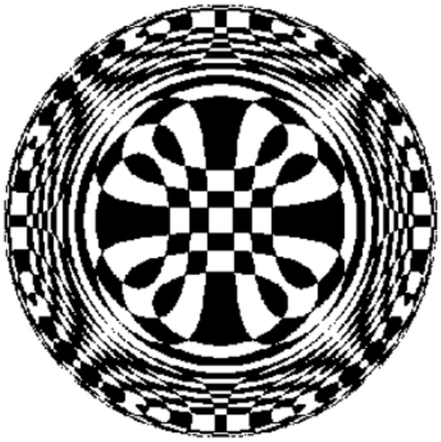

Fig. 2. Example of zone distribution for an aspheric element with mostly aspherical aberration. Each interferogram is generated by a specific source of the array.

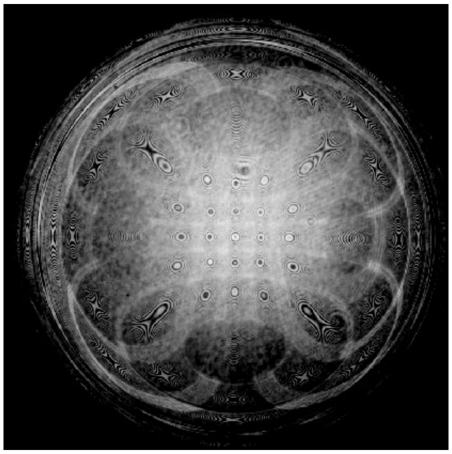

Fig. 3. Example of the distribution of zone interferograms for an aspheric element.

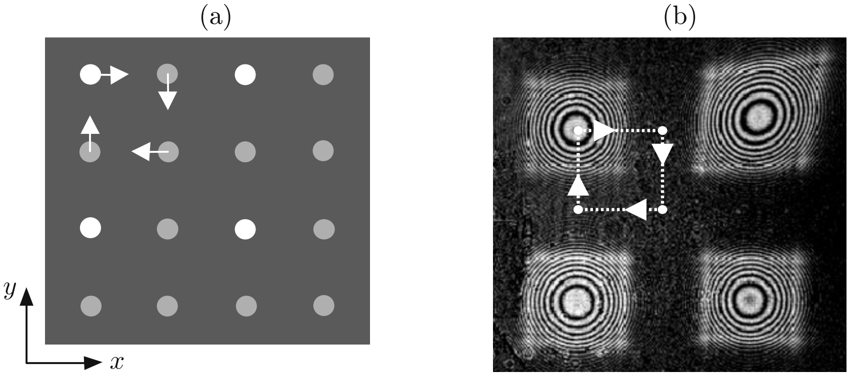

Fig. 4. Measurement sequence: (a) movement of the selection mask over the source array in the x and y directions (the sources indicated with white are active sources); (b) interferogram sequence as seen on the camera. The interferograms correspond to the active sources shown in Fig. 4a.

reference (upper path) and test beam (lower path) by the beam splitter BS_1. A diffractive optical element point source array (PSA), consisting of a microlens array (MA) on the front side and a matching pinhole array (PA) on the backside of the element fabricated together in a monolithic package, is placed in the test path of the interferometer. This element generates a two-dimensional matrix of point sources that constitute the test beams of the interferometer. The lens L_2 collimates these sources, thus generating a set of wavefronts with different tilts. For an asphere that contains a spherical basic shape, it is advantageous to use an additional transmission sphere O to compensate this spherical component of the wavefront. If planar aspherical surfaces were considered (e.g., Schmidt-plate geometry) the transmission sphere would not be necessary. After reflection on the asphere, the wavefront is imaged by lens L_3 onto the detector C. The lens L_1 focuses the beam from the upper branch of the interferometer (reference wave) in the aperture B and generates a plane wave after lens L_3 which interferes with the test beam reflected from the asphere. As usual, in the Fourier plane of the imaging optics, an aperture B is positioned in order to eliminate those components of the test beam which lead to irresolvable fringes (subsampling) on the detector C.

Because the technique performs the measurement violating the null-test condition, strong retrace errors contributions to the measured wavefront are expected. As previously mentioned, this implies that the calibration of the interferometer to separate the contributions of the interferometer itself and the surface to be measured is an unavoidable step of the measurement procedure. Since the complete characterization of each single element that the interferometer contains is extremely complex and time-consuming [16] (fabrication parameters, positioning, etc.), a new method has been implemented [17, 1, 15] to avoid this tedious procedure.

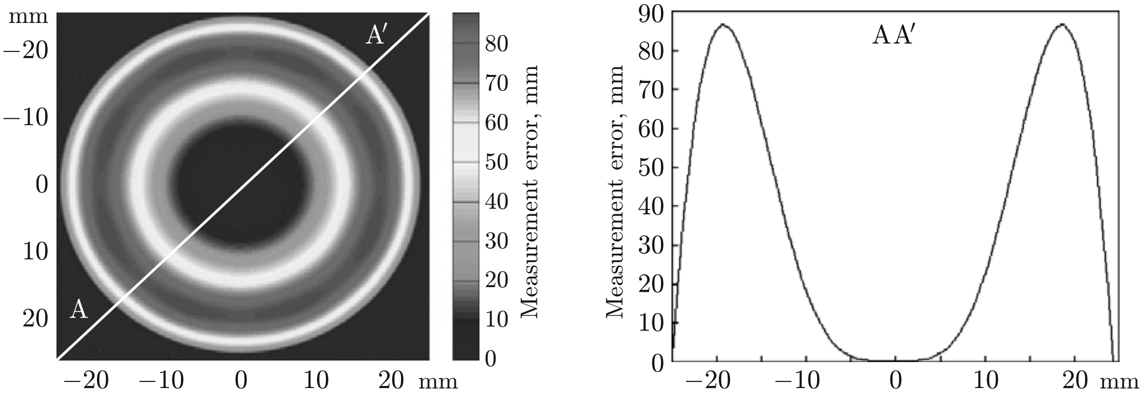

Fig. 5. Experimental results: (a) the remaining error after calculation of the surface profile from the measurements amounts to approximately $\sim$0.13λ PV; (b) cut along the line AA' of the two-dimensional map shown in Fig. 5a.

The main idea is to characterize the aberrations of the wavefronts propagating to the test space (the volume where the test surface is positioned) and from the test space to the detector. For each source of the array, we position a reference sphere in the test space of the interferometer such that the number of fringes on the detector will be minimized. For that purpose, a precise air bearing translation stage made by Aerotech (USA) is used. The measured wavefronts and sphere positions are then used in combination with the nominal design of the interferometer in an optimization process. The result is a set of parameters that describe the aberrations of the system for all possible propagation directions through the interferometer. Once we are able to systematically calculate the aberrations introduced by the interferometer, we can also calculate the expected interferogram for a given asphere prescription. At this stage an additional optimization process takes place. Corrections for each of the parameters that describe the aspheric surface are calculated until they match the measured phase on the detector.

It is important to mention that adjacent light sources generate interferograms which correspond to adjacent areas on the asphere. Due to diffraction effects at the edge and overlapping, a pitch between the individual sub-interferograms is desired. Thus, each source generates a group of zones covering different parts of the test element. An example of such zone arrangement is depicted in Fig. 2. Figure 3 shows the sub-interferograms for the central domain of the asphere while Fig. 4 illustrates the measurement sequence.

As an example, a rotationally symmetric asphere with a deviation of approximately 900 μm from its best-fit sphere and 1 μm deviation from its design prescription was measured experimentally with the proposed interferometer. A source array with $15 \times 15 = 225$ sources and a spacing of 2.5 mm between them was used. We generated each source with microlenses with a numerical aperture of 0.2 and a pinhole of size 30 μm. A JenFizar 4″ (aperture ratio 0.75; numerical aperture 0.67) transmission sphere was used to compensate for the spherical component of the wavefront, as previously explained. The detector was a 4 megapixel CCD-camera with a pixel pitch of 7.4 μm.

For the calibration, we used a reference sphere with an accuracy of $\lambda/20$ and almost 90 calibration positions. The results are shown in Fig. 5. The achieved measurement accuracy is on the order of $\sim$0.13λ peak-to-valley (PV). Further improvement is on the way to ensure finally $\lambda/30$ PV. The current accuracy of the system is limited by the mechanical stability of this first demonstrator setup. We crosschecked these results with measurements obtained using a computer-generated hologram calculated for the asphere. It is important to note that the optimization algorithm provides corrections to the polynomial description of the asphere. High frequency details of the surface are not modeled by this approach. Hence, an additional step is required in which we calculate the difference between the measured phase and the one expected from the shape of the asphere obtained from the optimization.

TESTING ASPHERIC SURFACES WITH A CHROMATIC FIZEAU INTERFEROMETER

In current interferometric systems, the central wavelength typically is kept constant with high accuracy, or sometimes used as means to implement phase shifting or control the coherence properties. However, the

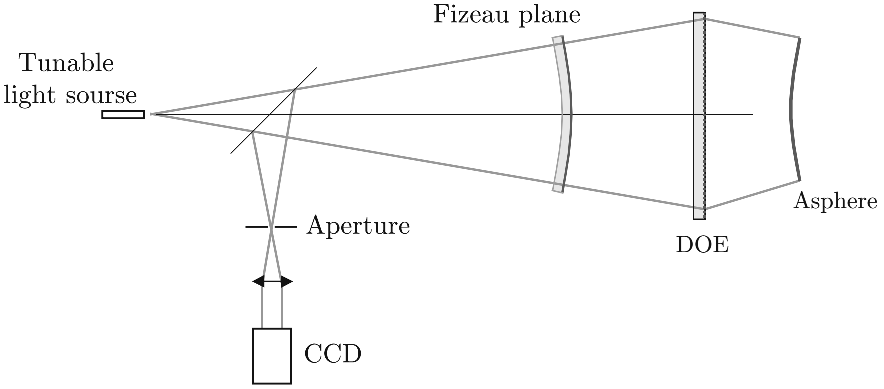

Fig. 6. Chromatic Fizeau interferometer. The adaptation of the wavefront is done by a diffractive optical element. Because diffraction is wavelength dependent, different areas of the test asphere are measured for different wavelengths.

Table 1. Parameters of the four EUV aspheres which should be measured in one setup

Asphere No.	Diameter, mm	Spherical radius, mm
1	200	400
2	460	−550
3	100	200
4	300	−260

wavelength can be tuned without mechanical movement in the measurement setup and the exact wavelength can be determined dynamically with an accuracy of 10^{-6}. The idea of the presented approach is to use the wavelength for the flexibilization of asphere metrology. Here we propose a chromatic Fizeau interferometer where the static laser is replaced by a tunable coherent light source [4].

Figure 6 shows the measurement setup with a diffractive optical element (DOE) as null optic. Due to the principal similarity to standard Fizeau setups, experiences with the monochromatic Fizeau interferometer can be directly adopted. At the camera, the test beam and the reference beam which is reflected from the Fizeau plane in the cavity interfere. Because this is to a large extent a common-path setup, disturbances in the cavity have the same effect on both beams and do not disturb the measurement.

The coherence length of the laser has to be long enough to span twice the radius dependent path difference between Fizeau plane and asphere. Optionally, an external cavity is needed to adjust the path differences. In this case, one bit of the dynamic range of the camera is lost due to the incoherent background light. A titan–sapphire laser meets the demands of high beam quality, coherence length, and wavelength adjustability larger than 100 nm. In the following simulations, a Sirah Matisse (Germany) titan–sapphire laser [18] is used, which offers a tunable range of $\lambda = 740$–880 nm with the same mirror set.

Depending on the wavelength, the diffraction angle at the DOE and hence the incidence angle at the asphere change. Figure 7 shows the wavelength dependent diffraction angle of this laser. At 500 line pairs per millimeter, the angle can be adjusted to $\sim 5^\circ$. The idea is to measure the asphere with a set of different wavelengths. With each wavelength, a different part of the asphere can be measured in a null test environment. If the asphere is radially symmetric, this means that with each wavefront another ring zone can be measured.

Measurement of EUV Aspheres

To demonstrate the measurement principle, we show the simulation of the measurement of four aspheres for future EUV lithography systems. All aspheres can be measured in one setup. The industrial requirements of such a measurement setup are stable implementation in the production process, a measurement interval within minutes, measurement errors below 0.2 nm RMS, and a minimal lateral resolution of 1000 pixel over the diameter. Because of the manufacturing cost of the DOE, the line density should be below 550 line pairs per millimeter and the maximal diameter of the diffractive element should not exceed 105 mm. The

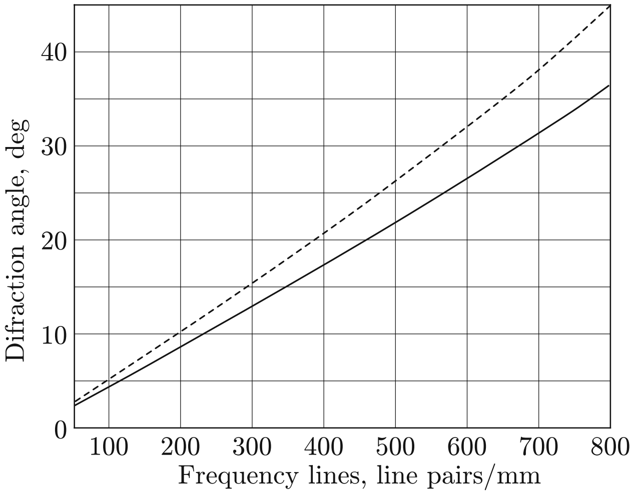

Fig. 7. Diffraction angle versus line density of the DOE (the solid and dashed curves correspond to $\lambda = 740$ and 880 nm, respectively).

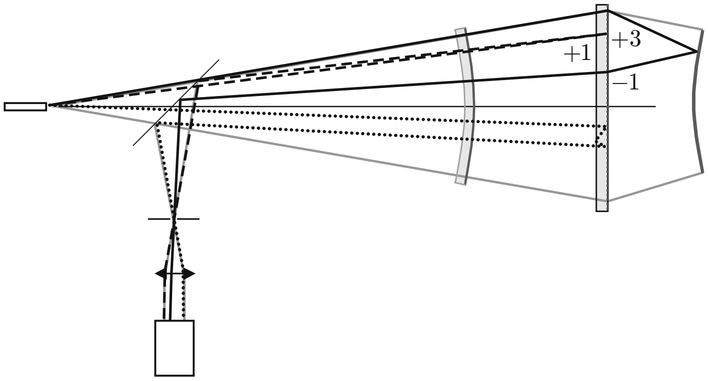

Fig. 8. Unwanted light paths which contribute to the measurement error. Diffraction combinations like (+3/−1) (solid line), single reflections (dashed line), and double reflections (dotted line) interfere with the measurement signal because they are not filtered at the aperture.

dimensions of the four EUV aspheres are shown in Table 1. Because the exact aspheric form is not important in this study of the measurement principle, we will use primary spherical aberration to simulate the aspheric form. The number of measurements with different wavelengths can be calculated analytically [19], where A is the asphericity, λ is the central wavelength, and N is the maximum number of fringes allowed in one measurement:

$$\text{Number of measurements} = \frac{64A}{3\lambda N}\,. \tag{1}$$

The zone width decreases quadratically with increasing radius. The smallest zone can be calculated with the number of pixels P over the aperture:

$$\text{Minimal zone } = \frac{PN\lambda}{128A}\,. \tag{2}$$

For the measurement of a test asphere with an asphericity of 20 μm, $\lambda = 0.81$ μm, $P = 2000$, and a maximal number of $N = 10$ fringes, 53 measurements are needed for a complete measurement. The minimal zone width is then 6 pixel. To find a setup for the measurement of all aspheres the following parameters have to be considered: the position of the DOE, the distance between DOE and asphere, the focal length of the image system, the resolution of the CCD, the radius and line density of the DOE, the numerical aperture and tuneable wavelength range of the laser source. The goal is to find a setup where all parameters except wavelength and distance between DOE and asphere are constant. After the measurement of one asphere is finished, the next asphere has to be aligned. Therefore, the distance between DOE and

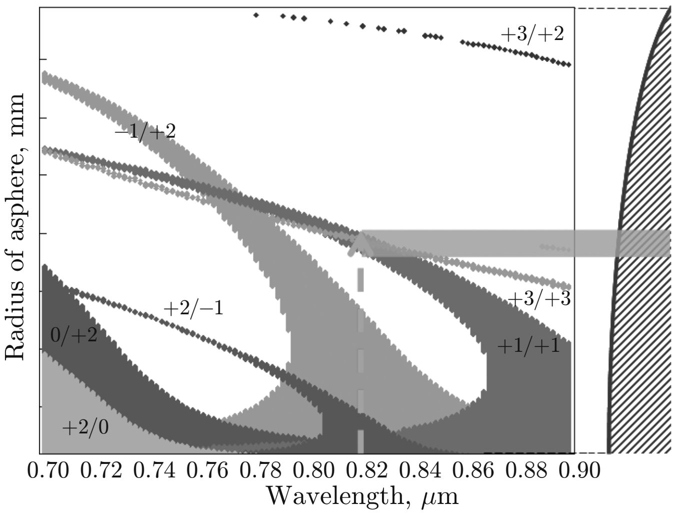

Fig. 9. Example of the distribution of the wanted combination order $(+1/+1)$ and a small selection of unwanted diffraction orders along the radius of an asphere. On the right side a sketch of the asphere is shown. The measurement is disturbed by the diffraction order combination $(+3/+3)$ for example at 820 μm.

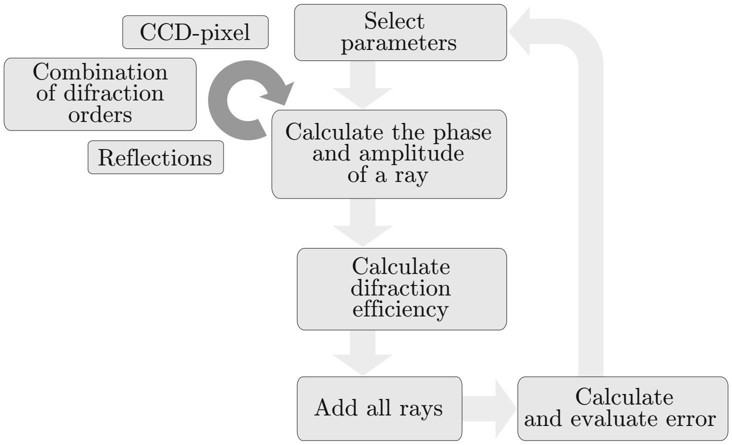

Fig. 10. Block diagram for the optimization of the measurement parameters with respect to measurement errors.

asphere can change for each asphere and is bound by geometric constraints and the size of the DOE. Concave aspheres will be measured in the minus first diffraction order. For concave asphere radii larger than the DOE, a minimal distance between DOE and asphere has to be kept to illuminate the full asphere. Below that distance, the asphere cannot be measured over the whole radius. Convex aspheres will be measured in the plus first diffraction order. For small convex aspheres, there is a maximal distance between DOE and asphere.

The dependencies of the measurement parameters with their restrictions are complex. To find the parameter space where the measurement of all four aspheres is possible, we implemented a program to screen all possible parameter combinations. The next step is to examine the remaining parameter space for the parameter set that promises the smallest measurement errors. As mentioned above, the desired combination of diffraction orders for a convex asphere is the plus first order on the way to the asphere and it is the plus first order on the way back $(+1/+1)$. Unfortunately, other combinations of diffraction orders contribute to the interferogram (Fig. 8). The solid line represents an example of an unwanted diffraction order combination $(+3/-1)$ which is not blocked by the aperture. Because of the high demands on the measurement accuracy, even high diffraction orders have to be considered. A distribution of a small selection of diffraction orders for an asphere is shown in Fig. 9. In this case, the combination $(+3/+3)$ and $(-1/+2)$ among

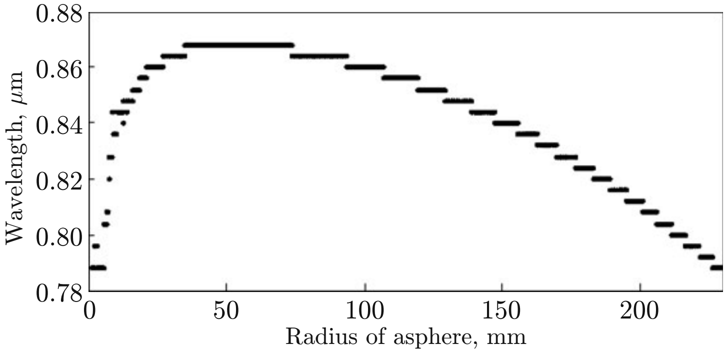

Fig. 11. Wavelength versus radial zone of an asphere.

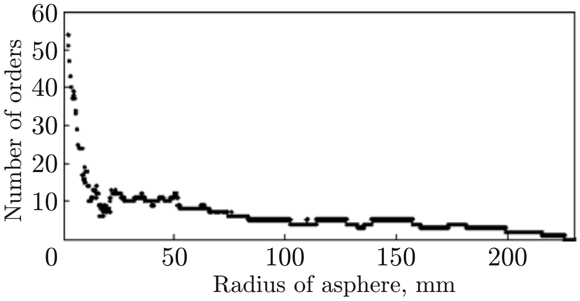

Fig. 12. Distribution of unwanted diffraction orders along the radius of asphere No. 2.

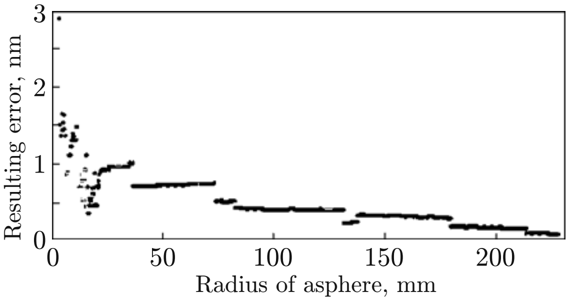

Fig. 13. Resulting measurement error for asphere No. 2.

the shown diffraction orders disturb the measurement. Other unwanted effects are reflections at different optical surfaces, reflected diffraction orders (dashed line) at the DOE, and their combinations (dotted line) (see Fig. 8).

For a given set of measurement parameters, the resulting errors due to unwanted diffraction orders and reflections have to be calculated. A block diagram of the algorithm for calculating the measurement errors are shown in Fig. 10. The ray tracing is done with the optical design program ZEMAX [20]. The simulation takes advantage of the radial symmetry of the aspheres. Each ray is calculated for each possible diffraction order combination and reflections. We have considered all orders up to 20th order. The framework, selection of input parameters, and analysis of the calculated data are done in MATLAB.

The following example of a simulation analysis for asphere No. 2 is representative for the other three aspheres. The distance from the laser to the DOE in this setup is 1100 mm. The distance between the DOE and the asphere is a free parameter. The following analysis is done with a distance of 333 mm, because simulations showed that the measurement errors can be kept minimal at this distance.

Simulation Analysis for Asphere No. 2

Figure 11 shows the correlation between wavelength and radial zone which can be measured. Only a part of the tunable wavelength range of the laser is used (740–870 nm). The distribution of unwanted diffraction orders along the radius is drawn in Fig. 12. The number of error sources increases near the optical axis. The resulting measurement error is not a linear function of the number of unwanted diffraction orders. The reason is the varying intensity of the individual order combinations due to the different diffraction efficiencies at the DOE. This can be seen in Fig. 13. The calculated measurement error increases near the optical axis, too. The reason is shown in Fig. 14. For this measurement setup, the most significant combination of diffraction orders is a high negative order on the way to the asphere and zero order diffraction on the way back. This kind of measurement error can be removed by a small blocking aperture on the optical axis. Both the number of unwanted diffraction orders in Fig. 15 and the resulting measurement error in Fig. 16 are effectively reduced. In this configuration, the errors are small enough to meet the measurement requirements defined in the beginning.

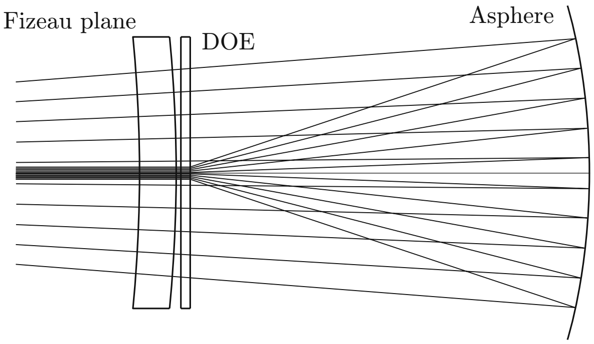

Fig. 14. Illustration explaining an increase in the measurement error near the optical axis.

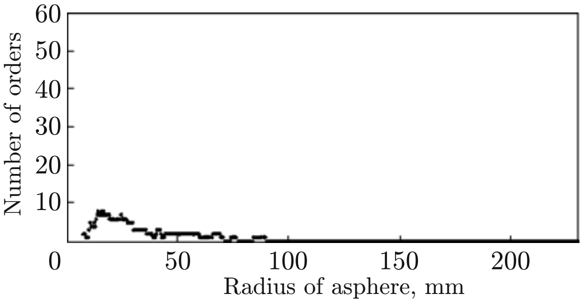

Fig. 15. Reduction in the number of unwanted diffraction combinations by using a small blocking aperture on the optical axes (radius 3 mm).

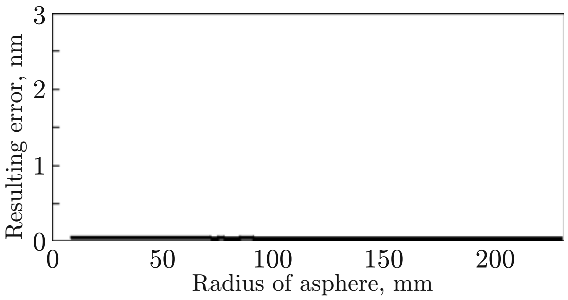

Fig. 16. Resulting measurement error due to the use of a blocking aperture on the optical axis.

Measurement Configurations for All Four Aspheres

Equivalent to the approach for asphere No. 2, the measurement parameters for the other three aspheres can be determined. The configurations of all aspheres are shown in Fig. 17. The smallest and largest wavelength to measure the asphere is drawn. As noted above, the measurable zone widths decrease with increasing radius. Therefore, the smallest zone is located at the maximal radius. No change in the setup is required to switch to a different asphere, and only the distance between DOE and asphere changes. This is advantageous because the interferometer does not need to be calibrated for each new asphere. Asphere No. 1 is particularly hard to measure. The diameter allows only a small position variation of the asphere to minimize measurement errors.

There are other possible ways to reduce the influence of unwanted diffraction orders. Using a larger DOE enables more freedom for the position of the asphere. The computational removal of disturbances is complex but in principle possible since their position, intensity, and phase can be calculated. An iterative algorithm seems promising for the correction. A reduction of the error influence due to diffraction orders can also be obtained by using different positions of DOE or asphere for one measurement; however, this would break the desirable property of no moving parts.

All aspheres need a small blocking aperture on the optical axis. This is comparable to the monochromatic Fizeau interferometer in which the measurement values near the optical axes are inaccurate due to reflections. The lateral resolution on an asphere using a 4 megapixel camera, the required wavelength range, and the unevaluable central radius are shown in Table 2.

CONCLUSIONS

We presented two new techniques for the testing of surfaces by optical metrology. In the first case, a novel interferometer for the characterization of steep aspheric wavefronts coming from optical surfaces was introduced. Due to the inherent parallelization resulting from the use of multiple sources, the full-field measurement of a surface can be performed extremely fast in comparison to other techniques. The interferometer configuration was designed to characterize elements with up to 1000 μm SAG deviation and

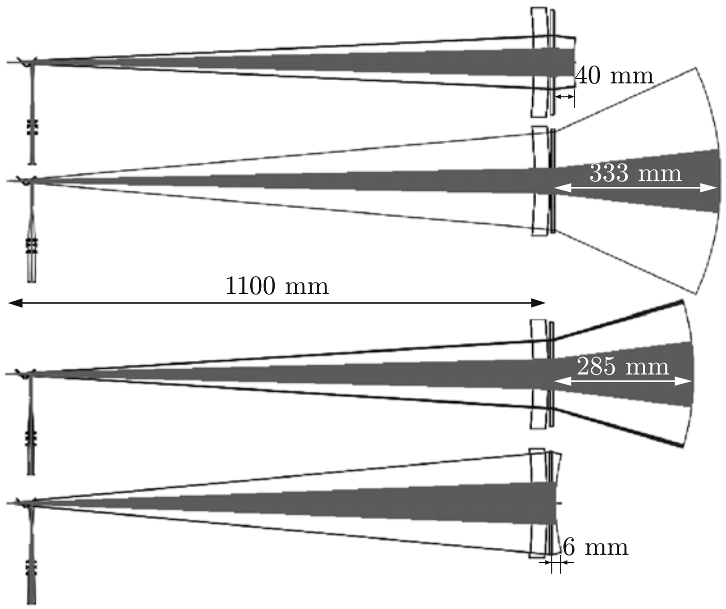

Fig. 17. Resulting measurement configurations for four aspheres.

Table 2. Parameters and results for the measurement of four EUV aspheres

Asphere number	Distance between DOE and asphere, mm	Image radius, mm	Lateral resolution (aperture diameter $d = 3.5$ mm), mm/pixel	Wavelength range, nm	Not evaluable central radius, mm
1	25.0	7.1	0.29	744–770	3
2	333.0	7.0	0.70	788–880	3
3	40.0	3.8	0.28	774–733	4
4	282.5	5.0	0.64	754–782	10

±10° slope deviation with an aimed accuracy of $\lambda/30$ PV. The current accuracy of the system is limited to 0.13λ due to the mechanical stability of this first demonstrator setup. The chromatic Fizeau interferometer is based on the well-known monochromatic method. The profound experience with the construction and operation of such a measurement system can be directly transferred in many aspects to this new type of measurement system. But the chromatic variant is far more flexible. In [4, 19], it was shown that the measurement of at least four different aspheres is possible in one setup.

Financial support from the Bundesministerium Bildung, Forschung und Technologie (FKZ 13N8742) as well as from our industrial partners “Jenoptik L.O.S.” and “Zeiss/SMT” is gratefully acknowledged for the testing of aspheres with increased flexibility.

REFERENCES

1. E. Garbusi, C. Pruss, J. Liesener, and W. Osten, “New Technique for Flexible and Rapid Measurement of Precision Aspheres,” Proc. SPIE **6616**, 661629-1–661629-11 (2007).
2. C. Pruss, E. Garbusi, and W. Osten, “Testing Aspheres,” Opt. Photon. News **19** (4), 24–29 (2008).
3. E. Garbusi, C. Pruss, and W. Osten, “Novel Interferometer for Precise and Flexible Asphere Testing,” Opt. Lett. **33** (24), 2973–2975 (2009).
4. L. Seifert, C. Pruss, B. Dörband, and W. Osten, “Measuring Aspheres with a Chromatic Fizeau Interferometer,” Proc. SPIE **7389**, 738919-1–738919-9 (2009).
5. J. C. Wyant and P. K. O’Neill, “Computer Generated Holograms: Null Lens Test of Aspheric Wave-Fronts,” Appl. Opt. **13** (12), 2762–2765 (1974).

6. C. Pruss, S. Reichelt, H. J. Tiziani, and W. Osten, "Computer-Generated Holograms in Interferometric Testing," Opt. Eng. **43** (11), 2534–2540 (2004).
7. A. G. Poleshchuk, V. P. Korol'kov, V. V. Cherkashin, S. Reichelt, and J. Burge, "Methods for Minimizing the Errors in Direct Laser Writing of Diffractive Optical Elements," Avtometriya **38** (3), 3–19 (2002) [Optoelectr., Instrum. Data Process. **38** (3), 3–15 (2002)].
8. P. Murphy, J. Fleig, G. Forbes, et al., "Subaperture Stitching Interferometry for Testing Mild Aspheres," Proc. SPIE **6293**, 62930J (2006).
9. M. F. Küchel, "Absolute Measurement of Rotationally Symmetrical Aspheric Surfaces," in *OSA Topical Meeting on Optical Fabrication and Testing, Rochester, USA, 2006.*
10. J. E. Greivenkamp, "Sub-Nyquist Interferometry," Appl. Opt. **26** (24), 5245–5258 (1987).
11. J. E. Greivenkamp and R. O. Gappinger, "Design of a Non-Null Interferometer for Aspheric Wave Fronts," Appl. Opt. **43** (27), 5143–5151 (2004).
12. Y.-M. Liu, G. N. Lawrence, and C. L. Koliopoulos, "Subaperture Testing of Aspheres with Annular Zones," Appl. Opt. **27** (21), 4504–4513 (1988).
13. M. Melozzi, L. Pezzati, and A. Mazzoni, "Testing Aspheric Surfaces Using Multiple Annular Interferograms," Opt. Eng. **32** (5), 1073–1079 (1993).
14. J. Liesener and H. J. Tiziani, "Interferometer with Dynamic Reference," Proc. SPIE, **5252**, 264–271 (2004).
15. J. Liesener, E. Garbusi, C. Pruss, and W. Osten, DE Patent No. 10 2006 057 606, Verfahren und Messvorrichtung zur Vermessung Einer Optisch Glatten Oberfläche (November 24, 2006).
16. R. O. Gappinger and J. E. Greivenkamp, "Iterative Reverse Optimization Procedure for Calibration of Aspheric Wave-Front Measurements on a Nonnull Interferometer," Appl. Opt. **43** (27), 5152–5161 (2004).
17. J. Liesener, Zum Einsatz räumlicher Lichtmodulatoren in der interferometrischen Wellenfront-messtechnik. PhD Thesis (Univ. Stuttgart, Stuttgart, 2007).
18. *Sirah Matisse Titan Saphire Laser*; http://www.sirah.com/.
19. L. Seifert, Flexible Verfahren zur Vermessung asphärischer Flächen, PhD Thesis. (Univ. Stuttgart, Stuttgart, 2009).
20. *Optical Design Program ZEMAX*; http://www.zemax.com/.